Chemical Science

ROYAL SOCIETY OF CHEMISTRY

EDGE ARTICLE

View Article Online
View Journal | View Issue

Check for updates

Cite this: *Chem. Sci.*, 2024, **15**, 13082

All publication charges for this article have been paid for by the Royal Society of Chemistry

Received 27th May 2024
Accepted 12th July 2024

DOI: 10.1039/d4sc03445g

rsc.li/chemical-science

A novel NIR fluorescent probe for copper(II) imaging in Parkinson's disease mouse brain†

Jianmei Chen,[a] Rongqing Luo,[a] Shuang Li,[a] Jinping Shao,[a] Ting Wang,[a] Shumei Xie,[a] Li Xu,*[ac] Qiuyun You,*[acd] Shumin Feng *[ac] and Guoqiang Feng *[b]

Abnormal copper ion (Cu^{2+}) levels are considered to be one of the pathological factors of Parkinson's disease (PD), but the internal relationship between Cu^{2+} and PD progression remains elusive. Visualizing Cu^{2+} in the brain will be pivotal for comprehending the underlying pathophysiological processes of PD. In this work, a near-infrared (NIR) fluorescent probe, **DDAO-Cu**, capable of detecting Cu^{2+} with exceptional sensitivity (about 1.8 nM of detection limit) and selectivity, rapid response (<3 min), and deep tissue penetration, was designed for quantification and visualization of the Cu^{2+} level. It could detect not only Cu^{2+} in cells but also the changes in the Cu^{2+} level in the rotenone-induced cell and zebrafish PD models. Moreover, **DDAO-Cu** can cross the blood–brain barrier to image Cu^{2+} in the brain of PD model mice. The imaging result showed a significant increase in Cu^{2+} levels in brain regions of PD model mice, including the cerebral cortex, hippocampus, and striatum. Meanwhile, Cu^{2+} levels in the substantia nigra region were significantly reduced in PD model mice. It revealed the nuanced relationship of Cu^{2+} levels in different brain regions in the disease and indicated the pathological complexity of PD. Overall, **DDAO-Cu** represents a novel and practical tool for investigating Cu^{2+}-related physiological and pathological processes underlying Parkinson's disease.

Introduction

Parkinson's disease (PD) ranks as the second most prevalent neurodegenerative disorder, characterized by the specific loss of dopaminergic neurons in the substantia nigra (SN) and striatum (STR).[1] Predominantly affecting the motor system, particularly among the elderly population, PD presents with symptoms such as bradykinesia, muscle rigidity, resting tremor, and postural instability.[2,3] Despite notable progress in understanding PD, its precise pathogenesis remains elusive, posing challenges for accurate diagnosis and treatment. However, emerging evidence underscores a correlation between copper homeostasis and neuroinflammation in PD.[4] Copper ions (Cu^{2+}) can exacerbate α-synuclein aggregation in the substantia nigra, trigger mitochondrial dysfunction, and precipitate the degeneration of dopaminergic neurons, thereby hastening the progression of Parkinson's disease to a certain extent.[5,6] Although the level of Cu^{2+} in the cerebral cortex and cerebrospinal fluid (CSF) is significantly increased with the progression of PD,[7] due to the complexity of the brain system, the relationship between PD and Cu^{2+} still needs to be further explored. Therefore, developing a dependable and effective method for visualizing Cu^{2+} levels in PD models and clarifying the level of Cu^{2+} in PD is of great importance for understanding the pathogenesis of Parkinson's disease.

Several methods for detecting Cu^{2+} *in vivo* have been reported, including synchrotron radiation X-ray fluorescence,[8] photoacoustic imaging,[9] MRI[10] and fluorescence analysis.[11] Among these methods, fluorescence analysis stands out for its high sensitivity, and capability for high spatial and temporal resolution imaging,[12] especially near-infrared (NIR) fluorescence, which can minimize autofluorescence interference, enabling deep tissue penetration[13] and rendering it ideal for the *in situ* and real-time detection of various biomolecules in PD mice. Numerous NIR probes have been developed to detect reactive oxygen species (ROS), biothiols, hydrogen sulfide (H_2S), nitric oxide (NO), and α-synuclein aggregation,[14–18] contributing to the understanding of PD pathogenesis. However, due to NIR fluorescence characteristics, most NIR fluorescent probes have a large conjugated structure and high molecular weight, which makes it difficult to penetrate the blood–brain barrier (BBB) for *in situ* brain imaging *in vivo*.[19] In addition, due to the low Cu^{2+}

[a]*School of Pharmacy, Hubei University of Chinese Medicine, Wuhan 430065, China. E-mail: 2997@hbucm.edu.cn; 1471@hbucm.edu.cn; fsm3318@hbucm.edu.cn*

[b]*Key Laboratory of Pesticide and Chemical Biology of Ministry of Education, College of Chemistry, Central China Normal University, 152 Luoyu Road, Wuhan 430079, PR China. E-mail: gf256@mail.ccnu.edu.cn*

[c]*Hubei Shizhen Laboratory, Hubei University of Chinese Medicine, Wuhan 430065, China*

[d]*Engineering Research Center of TCM Protection Technology and New Product Development for the Elderly Brain Health, Ministry of Education, Wuhan 430065, China*

† Electronic supplementary information (ESI) available. See DOI: https://doi.org/10.1039/d4sc03445g

Open Access Article. Published on 22 July 2024. Downloaded on 1/15/2026 9:18:38 PM. This article is licensed under a Creative Commons Attribution-NonCommercial 3.0 Unported Licence.

© 2024 The Author(s). Published by the Royal Society of Chemistry

Open Access Article. Published on 22 July 2024. Downloaded on 1/15/2026 9:18:38 PM. This article is licensed under a Creative Commons Attribution-NonCommercial 3.0 Unported Licence.

level in the brain,[20] the design of turn-on NIR fluorescent probes capable of traversing the BBB for non-invasive detection of Cu^{2+} in the brain remains an immense challenge.

1,3-Dichloro-7-hydroxy-9,9-dimethylacridin-2(9*H*)-one (**DDAO**) serves as a NIR fluorophore with low molecular weight, high quantum yield (Φ = 0.39 in PBS buffer),[21] and extensive utility in fluorescent probe design for *in vivo* imaging. In this study, we present a novel colorimetric and NIR fluorescent probe, termed **DDAO-Cu** (Scheme 1).

This probe utilizes **DDAO** as the NIR fluorophore and incorporates a picolinate moiety as the reaction site for Cu^{2+}. Notably, **DDAO-Cu** exhibited remarkable selectivity and sensitivity (LOD = 1.8 nM) for the detection of Cu^{2+} in an aqueous solution (pH 7.4, HEPES buffer, 0.5% DMSO). Furthermore, **DDAO-Cu** demonstrated its utility for the first time in illustrating the overproduction of endogenous Cu^{2+} in cellular and zebrafish PD models. And finally, **DDAO-Cu** exhibited good blood–brain barrier permeability and tremendous ability for *in situ* real-time detection of Cu^{2+} in PD cells and animal models. To our knowledge, **DDAO-Cu** is the first reported turn-on NIR fluorescent probe capable of detecting Cu^{2+} in PD models, providing further insights into the elevated Cu^{2+} levels observed in PD.

Experimental

Instruments and materials can be found in the ESI.†

Synthesis of DDAO-Cu

DDAO (184 mg, 0.6 mmol) and Et_3N (204 mg, 1.2 mmol) were dissolved in dry DCM (30 mL), and then 2-pyridinecarbonyl chloride (170 mg, 1.2 mmol) was added. After stirring for about 2 h, the solvent was removed, and the crude powder was washed with mixed solvent (PE/THF 6 : 1, v/v) twice to afford **DDAO-Cu** as a yellow solid (102 mg, yield 41%). Mp: 178–179 °C. ^{1}H NMR (400 MHz, $CDCl_3$) δ 8.88 (d, J = 4.6 Hz, 1H), 8.31 (d, J = 7.7 Hz, 1H), 8.01–7.94 (m, 1H), 7.74 (d, J = 8.6 Hz, 1H), 7.67 (s, 1H), 7.62 (dd, J = 7.6, 4.8 Hz, 1H), 7.43 (d, J = 2.3 Hz, 1H), 7.34 (dd, J = 8.6, 2.2 Hz, 1H), 1.91 (s, 6H). ^{13}C NMR (101 MHz, $CDCl_3$) δ 173.19, 163.43, 153.45, 150.25, 149.96, 146.86, 140.29, 139.53, 139.45, 138.80, 137.41, 135.60, 133.14, 127.85, 126.10, 121.67, 120.08, 39.12, 26.60. ESI-MS: m/z found 413.2 ($M + H^+$). HR-MS (ESI): calcd for $C_{21}H_{15}Cl_2N_2O_3^+$ ($M + H^+$): 413.0454; found 413.0461.

Optical studies of DDAO-Cu for Cu^{2+}

Unless otherwise stated, all UV-vis and fluorescence spectra studies were performed at 37 °C in a 10 mM HEPES buffer (pH 7.4, with 0.5% DMSO) solution. The stock solution of **DDAO-Cu** (1 mM) was prepared in DMSO, and the concentration used for optical studies was maintained at 5 μM. Spectra were recorded 3 minutes after the addition of Cu^{2+} and other analytes. In the fluorescence collection, the excitation wavelength was set at 602 nm (slit width: d_{ex} = 2.5 nm, d_{em} = 5 nm).

Cytotoxicity evaluation

Rat pheochromocytoma (PC12) cell lines were purchased from Procell Life Science & Technology Co., Ltd and cultured in RPMI-1640 medium supplemented with 10% fetal bovine serum at 37 °C in a 5% CO_2/95% air incubator. The cytotoxicity of **DDAO-Cu** was evaluated by incubating in PC12 cells with 0–25 μM **DDAO-Cu** for 24 h using the MTT assays.[22]

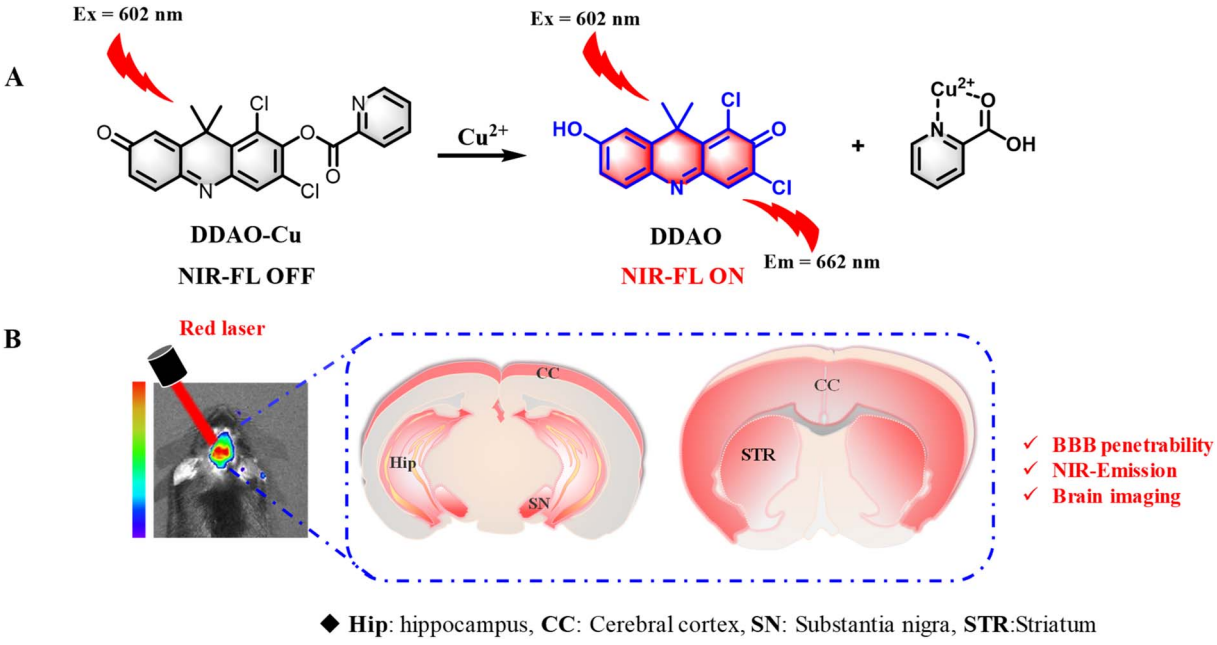

Scheme 1 (A) Fluorescent probe **DDAO-Cu** for the detection of Cu^{2+}. (B) Schematic illustration of imaging of Cu^{2+} in the PD mouse brain using DDAO-Cu.

Open Access Article. Published on 22 July 2024. Downloaded on 1/15/2026 9:18:38 PM. This article is licensed under a Creative Commons Attribution-NonCommercial 3.0 Unported Licence.

Cu^{2+} imaging in living cells

To image exogenous Cu^{2+}, PC12 cells were treated with Cu^{2+} (5, 10, and 20 μM) at 37 °C for 0.5 hours, followed by incubation with **DDAO-Cu** for 20 minutes without washing. To image endogenous Cu^{2+} in cells, the PD cells were incubated with 2,3-dimercaptopropane-1-sulfonic acid sodium salt (DMPS, a metal chelating agent, 300 μM) for 30 minutes, followed by the addition of 5 μM **DDAO-Cu** for 20 minutes, which served as the inhibition group. PC12 cells directly treated with **DDAO-Cu** (5 μM, 20 minutes) served as the experimental group. PC12 cells served as the blank group. For imaging Cu^{2+} in the cellular PD model, PC12 cells were treated with rotenone (1 μM) for 1 hour to establish the cellular PD model.[23] The PD cells directly treated with **DDAO-Cu** (5 μM, 20 minutes) served as the model group. Additionally, the PD cells were incubated with DMPS for 30 minutes, followed by the addition of 5 μM **DDAO-Cu** for 20 minutes, which served as the control group. PC12 cells directly treated with **DDAO-Cu** (5 μM, 20 minutes) served as the blank group. All cells were imaged without washing in the red channel ($\lambda_{ex}/\lambda_{em}$ = 561/620–680 nm). Subsequently, the cells were detached using trypsin digestion, collected, washed with PBS three times, resuspended in 400 μL PBS, and subjected to flow cytometry.

Imaging the zebrafish PD model with DDAO-Cu

The zebrafish PD model was also established by rotenone stimulation.[24] The zebrafish were treated with rotenone (1 μM) for 1 hour to induce the zebrafish PD model. The experiment comprised three groups: (1) PD zebrafish incubated with 5 μM **DDAO-Cu** for 10 minutes; (2) PD zebrafish incubated with DMPS for 30 minutes, washed with PBS, followed by incubation with 5 μM **DDAO-Cu** for 10 minutes; (3) normal zebrafish incubated with 5 μM **DDAO-Cu** for 10 minutes. Subsequently, all zebrafish were fixed with 1% agarose and imaged in the red channel ($\lambda_{ex}/\lambda_{em}$ = 561/620–680 nm).

Establishing the PD mouse model using MPTP

l-Methyl-4-phenyl-l,2,3,6-tetrahydropyridine (MPTP) selectively induces dopaminergic neuronal damage in the substantia nigra and striatum, leading to a parkinsonian syndrome; the MPTP-induced PD model was the gold standard in PD research.[25] In our study, we utilized MPTP to establish the Parkinson's mouse model, and details of the timeline of the established experimental procedure and behavioural validation methods can be found in the ESI.†

In vivo imaging of the PD mouse model with DDAO-Cu

Before imaging, the fur was removed from the mouse's skull, followed by anaesthesia with 1% pentobarbital sodium (150 μL).

Tail-vein injection: PD mice and age-matched wild-type mice were then subjected to tail-vein injection of **DDAO-Cu** (50 μM, 100 μL) for different times (10–40 min) and imaged, respectively. For tetrathiomolybdate (TTM) group mouse, the PD mice were injected with TTM (100 μM, 100 μL) for 10 min, and then subjected to tail-vein injection of **DDAO-Cu** (50 μM, 100 μL) for different times (10–40 min) and imaged.

Brain injection: after mice were anesthetized, the mice were fixed on a brain stereotaxic apparatus. The scalp was cut and a hole was drilled at a certain position on the skull. **DDAO-Cu** (2.5 μM, 2 μL) was injected into the brain using a microinjector, and then the animal imaging was conducted at 10 min following injection of **DDAO-Cu**.

All the mice were imaged with a small animal fluorescence imager ($\lambda_{ex}/\lambda_{em}$: 600/660 nm).

Ex vivo fluorescence staining of DDAO-Cu to Cu^{2+} in mouse brain

PD mice and age-matched wild-type mice were intraperitoneally injected with 1% pentobarbital sodium and sacrificed at 30 min after injection. The brains were excised and soaked in formalin. The technical support of section production was from Hubei Biosci Biotech Co., Ltd. The sections of brain were stained with **DDAO-Cu** for 5 min. Subsequently, all sections were washed with PBS and the fluorescence observation was performed using a TCS SP8 (Leica, Germany) in the red channel ($\lambda_{ex}/\lambda_{em}$ = 561/620–680 nm).

Results and discussion

Probe preparation

DDAO-Cu was designed based on the Cu^{2+}-catalysed hydrolysis reaction of picolinate,[26] using **DDAO** as the NIR fluorophore and 2-pyridine carbonyl as both a recognition unit and a fluorescence quenching moiety. The route for the synthesis of probe **DDAO-Cu** is outlined in Scheme S1,† wherein **DDAO** underwent a reaction with 2-pyridinecarbonyl chloride to afford **DDAO-Cu** in 41% yield. The structure of **DDAO-Cu** was proved by NMR and mass spectroscopy (Fig. S1–S4, ESI†).

Detection of Cu^{2+} with DDAO-Cu

UV-vis and fluorescence spectra were employed to characterize the optical properties of **DDAO-Cu** for the detection of Cu^{2+}. Fig. 1 illustrates the absorption and fluorescence responses of **DDAO-Cu** to Cu^{2+} in HEPES buffer (pH 7.4) at 37 °C, Initially, **DDAO-Cu** exhibited an absorption maximum at 430 nm and very weak fluorescence at 662 nm (Φ = 0.011, using cresyl violet as the standard). Upon the addition of Cu^{2+}, the maximum absorption red-shifted to 602 nm (Fig. 1A), aligning well with the absorption maxima of **DDAO**, suggesting a conversion of **DDAO-Cu** to **DDAO** after the Cu^{2+} addition, with the conversion rate reaching 97%. Concurrently, Fig. 1B demonstrates a rapid increase in the fluorescence of **DDAO-Cu** at 662 nm, reaching saturation within 3 min after adding Cu^{2+}. Fluorescence kinetics demonstrated that the NIR fluorescence saturation occurred at approximately 100 s when the Cu^{2+} concentration was 10 μM (Fig. S5†), and the reaction displayed a pseudo-first-order with rate constant k_{obs} determined to be about 0.031 s^{-1}. This result indicates that **DDAO-Cu** can be used for rapid detection of Cu^{2+}. Notably, the remarkable colour changes of the **DDAO-Cu** solution from yellow to blue, accompanied by

© 2024 The Author(s). Published by the Royal Society of Chemistry

Open Access Article. Published on 22 July 2024. Downloaded on 1/15/2026 9:18:38 PM.
This article is licensed under a Creative Commons Attribution-NonCommercial 3.0 Unported Licence.

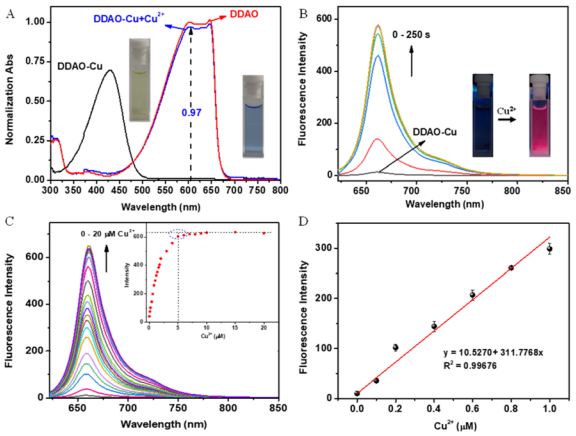

Fig. 1 (A) UV-Vis spectra of **DDAO** and **DDAO-Cu** (5 μM) before and after adding Cu^{2+} (10 μM). Inset: the color changes. (B) Fluorescence spectra change of **DDAO-Cu** (5 μM) upon addition Cu^{2+} (10 μM). Inset: the emission color changes under 365 nm light. (C) Fluorescence responses of **DDAO-Cu** (5 μM) upon increasing addition of Cu^{2+} (0–20 μM). Inset: intensity changes at 662 nm. (D) The linear relationship between fluorescence intensity changes at 662 nm with the concentration of Cu^{2+} (0–1 μM). Each data set was acquired 3 min after mixing. λ_{ex} = 602 nm, slit width: d_{ex} = 2.5 nm, d_{em} = 5 nm.

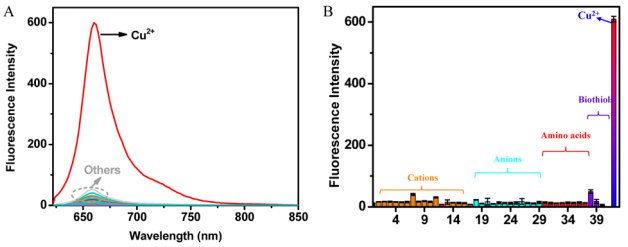

Fig. 2 (A) Fluorescence spectral changes and (B) fluorescence intensity (662 nm) changes of 5 μM **DDAO-Cu** for various analytes (100 μM unless stated otherwise) in HEPES buffer (pH 7.4, 10 mM) at 37 °C for 3 min. Analytes: (0) none, (1) Mn^{2+}, (2) Li^{+}, (3) Sr^{2+}, (4) Al^{3+}, (5) Sn^{2+}, (6) Cd^{2+}, (7) Ni^{2+}, (8) Zn^{2+}, (9) Fe^{2+}, (10) Fe^{3+}, (11) Hg^{2+}, (12) Na^{+}, (13) K^{+}, (14) Ca^{2+}, (15) Ba^{2+}, (16) NH_4^{+}, (17) SO_4^{2-}, (18) NO_3^{-}, (19) HSO_3^{-}, (20) CO_3^{2-}, (21) HCO_3^{-}, (22) F^{-}, (23) Cl^{-}, (24) Br^{-}, (25) I^{-}, (26) $S_2O_3^{2-}$, (27) $C_2O_4^{2-}$, (28) $C_3H_5O_3^{-}$, (29) AcO^{-}, (30) Leu, (31) Thr, (32) Gly, (33) Try, (34) Ser, (35) Tyr, (35) Phe, (37) Met, (38) Hcy, (39) Cys, (40) GSH (5 mM), (41) HS^{-}, and (42) Cu^{2+} (10 μM), λ_{ex} = 602 nm. d_{ex} = 2.5 nm, d_{em} = 5 nm.

bright red fluorescence (inset in Fig. 1A and B), indicate the feasibility of "naked-eye" detection of Cu^{2+}. These findings unequivocally establish **DDAO-Cu** as a promising turn-on NIR fluorescent probe for the rapid detection of Cu^{2+} in aqueous solution under mild conditions.

Under the optimal conditions, we investigated the sensitivity of **DDAO-Cu** in detecting Cu^{2+}. As depicted in Fig. 1C, the NIR fluorescence intensity at 662 nm exhibited a significant increase with the increasing concentration of Cu^{2+}, reaching saturation at 5 μM. Remarkably, even at low concentrations of Cu^{2+}, such as 0.1 μM (Fig. S6†), a substantial enhancement in the fluorescence signal was observed. Furthermore, **DDAO-Cu** exhibited good linear relationships in the range of 0–1.0 μM Cu^{2+} with R^2 = 0.99676 (Fig. 1D), and the limit of detection (LOD) was calculated to be 1.8 nM ($3\sigma/k$, S/N = 3), which is far below the clinically relevant range,[20] underscoring the remarkable sensitivity of **DDAO-Cu** to Cu^{2+}. In addition, the NIR fluorescence emission performance of **DDAO-Cu** enables deep tissue penetration, facilitating imaging of Cu^{2+} *in vivo*.

The selectivity of **DDAO-Cu** for Cu^{2+} was systematically evaluated. As shown in Fig. 2, despite the presence of various other analytes including cations (Mn^{2+}, Li^{+}, Sr^{2+}, Al^{3+}, Sn^{2+}, Cd^{2+}, Ni^{2+}, Zn^{2+}, Fe^{2+}, Fe^{3+}, Hg^{2+}, Na^{+}, K^{+}, Ca^{2+}, Ba^{2+}, and NH_4^{+}), anions (SO_4^{2-}, NO_3^{-}, HSO_3^{-}, CO_3^{2-}, HCO_3^{-}, F^{-}, Cl^{-}, Br^{-}, I^{-}, $S_2O_3^{2-}$, $C_2O_4^{2-}$, $C_3H_5O_3^{-}$, and AcO^{-}), amino acids (Leu, Thr, Gly, Try, Ser, Tyr, Phe, and Met), and biothiols (Hcy, Cys, GSH, and HS^{-}) at concentrations 10 times or even 500 times higher than that of Cu^{2+} (10 μM), negligible changes in fluorescence were observed. In stark contrast, a significant fluorescence response was elicited exclusively in the presence of Cu^{2+}, highlighting the exceptional selectivity of **DDAO-Cu** towards Cu^{2+}. Competition experiments further demonstrated that these potentially interfering analytes showed almost no interference with Cu^{2+} detection (Fig. S7a†). Additionally, the influence of pH was investigated (Fig. S7b†), revealing minimal fluctuations in the fluorescence intensity of **DDAO-Cu** across varying pH levels. However, upon the addition of Cu^{2+}, **DDAO-Cu** exhibited a notable fluorescence enhancement over a broad pH range. Remarkably, the optimal pH of **DDAO-Cu** in response to Cu^{2+} was around 7.4, indicating its aptness for detecting Cu^{2+} under physiological conditions and facilitating bioimaging of Cu^{2+}.

The design rationale behind **DDAO-Cu** entails the incorporation of 2-pyridine carbonyl which serves to disrupt the Intramolecular Charge Transfer (ICT) process of **DDAO**, resulting in the quenching of its fluorescence. Upon the addition of Cu^{2+}, a specific hydrolysis reaction with 2-pyridine carbonyl ensues, liberating a hydroxyl group and instigating a "turn-on" fluorescence response targeted at Cu^{2+}. The validity of this mechanism was confirmed through Job's plot analyses (Fig. S8a†), which revealed a 1 : 1 stoichiometry indicative of Cu^{2+}-promoted hydrolysis as a stoichiometric rather than catalyzed reaction by Cu^{2+}. Notably, the picolinic acid produced during the hydrolysis reaction strongly binds to Cu^{2+}, thus impeding its reactivity and providing further evidence in support of this mechanism. As shown in Fig. S8b,† the addition of Cu^{2+} to the **DDAO-Cu** solution in the presence of picolinic acid effectively hampers the hydrolysis of **DDAO-Cu**, underscoring the pivotal role of Cu^{2+} coordination to picolinic ester in facilitating the Cu^{2+}-promoted hydrolytic cleavage of **DDAO-Cu** to **DDAO**. These findings collectively elucidate a detailed recognition mechanism of **DDAO-Cu** for Cu^{2+}. Based on the above results, a detailed recognition mechanism of probe **DDAO-Cu** for Cu^{2+} was proposed as shown in Scheme S2.† The 2-pyridinecarbonyl group, endowed with strong electron-withdrawing ability, efficiently suppresses the fluorescence of **DDAO-Cu**. After the specific cleavage by Cu^{2+}, the ICT process of **DDAO-Cu** is reinstated, thereby enabling the "turn-on" NIR fluorescence analysis of Cu^{2+}. The confirmation of **DDAO** formation by LC-MS

© 2024 The Author(s). Published by the Royal Society of Chemistry

Open Access Article. Published on 22 July 2024. Downloaded on 1/15/2026 9:18:38 PM.
This article is licensed under a Creative Commons Attribution-NonCommercial 3.0 Unported Licence.

analyses (Fig. S9†) of the reaction mixture of **DDAO-Cu** and Cu^{2+} further corroborates the proposed reaction mechanism.

Imaging of Cu^{2+} in cellular and zebrafish PD models

Initially, the MTT method was employed to evaluate the cytotoxicity of **DDAO-Cu**, Notably, PC12 cells, a commonly utilized neural cell line for the study of PD,[27,28] exhibited robust cell viability (87%) even after 24 hour incubation with 25 μM **DDAO-Cu**, indicating its low cytotoxicity (Fig. S10†). Subsequently, the capability of **DDAO-Cu** for imaging Cu^{2+} in PC12 cells was investigated, with an increase in the concentration of Cu^{2+}, a gradual augmentation in red fluorescence was observed in the cells (Fig. S11†), suggesting the efficacy of **DDAO-Cu** in detecting exogenous Cu^{2+} in cellular environments. As shown in Fig. S12,† **DDAO-Cu** exhibits a weak fluorescent signal in PC12 cells, which is further diminished when the cells are pre-incubated with DMAP. This indicates the capability of **DDAO-Cu** to detect low levels of endogenous Cu^{2+}, highlighting its high sensitivity. Rotenone, known to induce oxidative stress and subsequent loss of dopaminergic neurons, is frequently employed to establish a highly reproducible model of PD.[29] Hence, rotenone was employed to stimulate PC12 cells; as depicted in Fig. 3, compared to the cell control (Fig. 3A), the PD model (Fig. 3B) exhibited notably heightened fluorescence. Moreover, preincubation of the PD model with DMPS resulted in a reduction in fluorescence intensity (Fig. 3C). These observations were further validated by flow cytometry experiments (Fig. 3E), confirming the intracellular accumulation of Cu^{2+} in the cellular PD model. Motivated by these findings, the fluorescence imaging performance was evaluated in the PD zebrafish model, which was also established using rotenone.[29] As illustrated in Fig. 4, rotenone-induced PD zebrafish displayed significantly elevated fluorescence compared to normal zebrafish. Moreover, fluorescence in the DMPS group was diminished, indicating a substantial increase in Cu^{2+} concentration in the zebrafish PD model. Collectively, these encouraging outcomes affirm the suitability of **DDAO-Cu** for monitoring

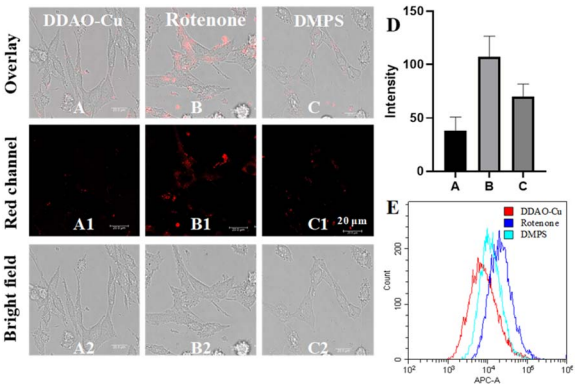

Fig. 3 (A) Cells were stained with **DDAO-Cu** for 20 min. (B) Cells were treated with rotenone (1 μM) for 1 h and then stained with **DDAO-Cu** for 20 min. (C) Cells were treated with rotenone (1 μM) for 1 h and DMPS (300 μM) for 30 min and then stained with **DDAO-Cu** for 20 min. (D) The fluorescence intensity of (A)–(C). (E) Flow cytometry data of (A1)–(C1). Red channel ($\lambda_{ex}/\lambda_{em}$ = 561/620–680 nm).

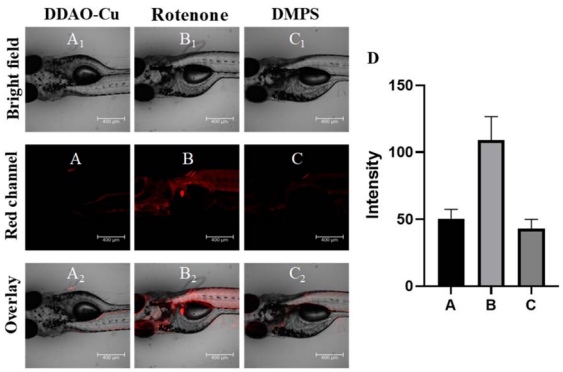

Fig. 4 Imaging of Cu^{2+} in the zebrafish PD model with **DDAO-Cu**. (A) Zebrafish were incubated with 5 μM **DDAO-Cu** for 10 min. (B) Zebrafish were incubated with 1 μM rotenone for 1 h, and then stained with 5 μM **DDAO-Cu** for 10 min. (C) Zebrafish were incubated with 1 μM rotenone for 1 h, then with 300 μM DMPS for 30 min, and then with 5 μM **DDAO-Cu**, for 10 min. (D) The intensity of (A)–(C). Red channel ($\lambda_{ex}/\lambda_{em}$ = 561/620–680 nm).

Cu^{2+} levels in both cellular and zebrafish PD models and reveal Cu^{2+} levels overexpressed in the PD model. Thus, **DDAO-Cu** can serve as an effective tool for the imaging and quantification of Cu^{2+}, which would be of great value for revealing the role of Cu^{2+} in PD.

Imaging of Cu^{2+} in the PD mouse model

Research indicates that MPTP treatment can induce PD mouse models, and the key characteristics of PD include motor dysfunction and the loss of dopaminergic neurons projecting to the STR and SN.[30–33] As illustrated in Fig. S13,† MPTP treatment prolonged the time for mice to descend in the pole test and suspension test compared to the W-T group. Additionally, in the novel object recognition test, the MPTP-treated group exhibited a significantly decreased latency to fall. The open field test was utilized to assess locomotor performance, revealing that mice injected with MPTP displayed significantly reduced total distance moved and increased resting time. These findings collectively demonstrate motor incoordination and dysfunction in MPTP-induced PD mice. Immunohistochemical analysis using Nissl staining was performed in the STR and SN,[34] as shown in Fig. 5, with more than 55% loss of nigral DA-ergic neurons in the SN, and 74% loss of DA-depletion in the STR in PD mice. Combined with the motor incoordination and dysfunction performance, these indicated that the PD mice were in the advanced presymptomatic stage.

To assess the BBB permeability of small molecules, a suitable oil–water partition coefficient (log *P*) in the range of 1–5 is considered one of the most important indicators.[35–37] First, the log *P* of **DDAO-Cu** was measured to be ~1.34 in the octanol–water system.[38] In addition, **DDAO-Cu** exhibits low molecular weight (MW: 412), and weak hydrogen bonding ability (no hydroxyl, carboxyl, and other groups); these properties would facilitate **DDAO-Cu** to cross the blood–brain barrier (BBB) and enrich in the brain. Then, we explored the feasibility of probe **DDAO-Cu** to image the brain *via* tail vein injection, and

© 2024 The Author(s). Published by the Royal Society of Chemistry

Open Access Article. Published on 22 July 2024. Downloaded on 1/15/2026 9:18:38 PM.
This article is licensed under a Creative Commons Attribution-NonCommercial 3.0 Unported Licence.

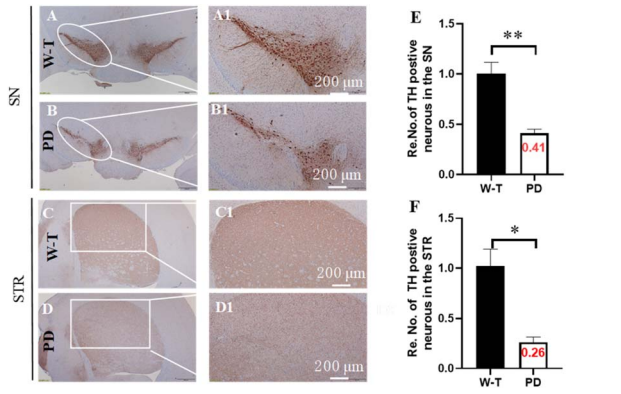

Fig. 5 (A–D) TH immunohistochemistry of SN and STR. (E and F) Relative quantifications of the TH immunohistochemistry positive neurons in the SN and STR from various groups, data are represented as the mean ± SD, $n = 3$, $^{*}P < 0.05$, $^{**}P < 0.01$.

fluorescence imaging in the brains of mice was performed for 40 min (Fig. 6A). As we can see, the fluorescence signal was enhanced in 10 min in the brain of PD mice, and with prolonging the time (>15 min), the signal faded away gradually (Fig. 6B), while the W-T mouse displayed a relatively weakly fluorescence, which faded away at 30 min. This indicates that **DDAO-Cu** can penetrate the blood–brain barrier and will be rapidly metabolized in the brain, possibly due to the good water solubility of **DDAO** and the active efflux mechanism of the BBB. After imaging, the mice were sacrificed, and the major organs, including the brain, kidney, lung, spleen, liver, and heart, were excised and imaged; as shown in Fig. S14,† the probe primarily accumulated in the liver and brain, and a small amount was found in the kidney, which may be because the brain has a high blood flow rate,[39] and **DDAO-Cu** was cleared from the body through hepatic and renal routes. This suggests that **DDAO-Cu** is suitable for low-residue and non-invasive detection of Cu^{2+} in the brain. Then, we conducted brain FL imaging in live mice with intact skulls. As shown in Fig. 6C, compared to the W-T mice, PD mice displayed brighter fluorescence (fluorescence increased by 1.5 times), however, when TTM (a copper ion chelating agent, which can cross the BBB)[40,41] was injected into the PD mice for 10 min, the fluorescence intensity was decreased, indicating that the Cu^{2+} level in PD mice was higher than that in W-T mice. To further indicate the elevated copper ions in the brain of PD mice, we had studied the Cu^{2+} content in mouse serum, and as shown in Fig. S15A,† few changes in fluorescence were observed between PD mice and W-T mice. And **DDAO-Cu** was injected into brain regions by intracranial injection; as shown in Fig. S15B,† the same result was found in the intracranial area compared to the control groups, which further suggests that the Cu^{2+} is overexpressed in the PD mouse brain.

Due to the complexity of the brain centers, the concentration of Cu^{2+} is different in different brain areas.[42] The highest concentration of Cu^{2+} was measured in the SN, and high levels of Cu^{2+} have also been detected in the hippocampus (Hip) and cerebral cortex (CC).[43] To further accurately assess the level of Cu^{2+} in the brain, the quantitative detection ability of **DDAO-Cu** in different brain tissues was investigated. At first, considering that the loss of dopaminergic neurons in the SN and STR is a key characteristic of PD, Cu^{2+} can precipitate the degeneration of dopaminergic neurons.[44,45] As illustrated in Fig. 7, compared with the PD group, stronger fluorescence in SN was observed in the W-T group, indicating low levels of Cu^{2+} in the SN of PD mice, which is consistent with the previously reported results.[46] This further confirms the imaging capability of **DDAO-Cu**. However, the higher fluorescence intensity was observed in the cortex, hippocampus, and striatum of PD mice (Fig. 7); this is attributed to the elevated copper ions in the cortex, hippocampus, and striatum during the advanced stages of PD.[47] In summary, the Cu^{2+} level in the SN of the PD mouse brain is

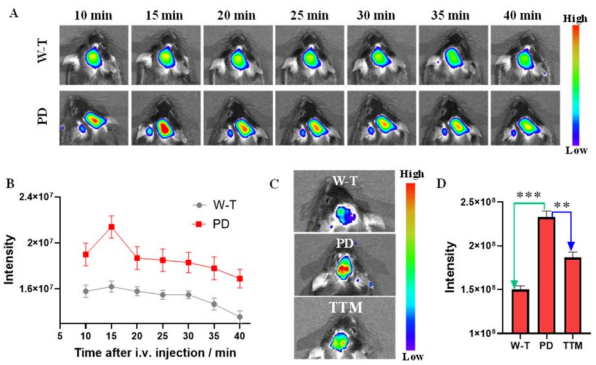

Fig. 6 (A) Imaging of C57 W-T mice and PD mice after injection of **DDAO-Cu** (50 μM, 100 μL) every 5 min within 40 min. (B) The fluorescence intensity of (A). (C) Imaging of mice after injection of **DDAO-Cu** for 10 min. (D) The fluorescence intensity of (C), data are represented as the mean ± SD, $n = 3$, $^{**}P < 0.01$. $^{***}P < 0.001$. $\lambda_{ex}/\lambda_{em}$ = 600/660 nm.

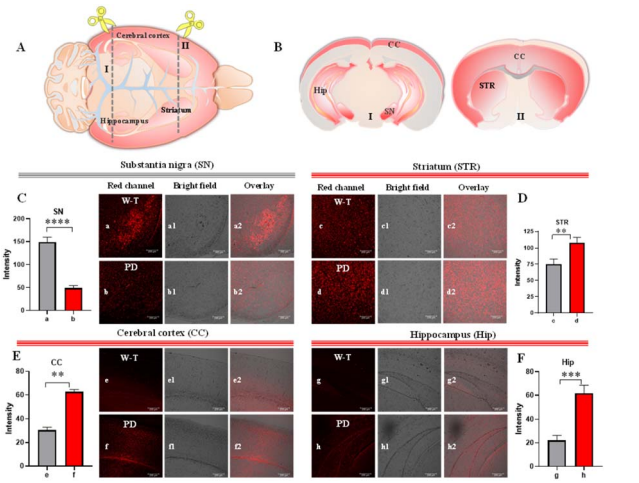

Fig. 7 *Ex vivo* fluorescence observation of brain slices from W-T and PD mice. (A) Schematic diagram of the brain. (B) Schematic diagram of the location of SN, Hip, CC and STR. (C–F) The fluorescence intensity and imaging of **DDAO-Cu** (5 μM) for 5 min in the SN (a, b), STR (c, d), CC (e, f), and Hip (g, h) regions, data are represented as the mean ± SD, $n = 3$, $^{**}P < 0.01$, $^{***}P < 0.001$. $^{****}P < 0.0001$. Red channel ($\lambda_{ex}/\lambda_{em}$ = 561/620–680 nm).

Open Access Article. Published on 22 July 2024. Downloaded on 1/15/2026 9:18:38 PM. This article is licensed under a Creative Commons Attribution-NonCommercial 3.0 Unported Licence.

reduced, accompanied by an increase in Cu^{2+} in the striatum, cerebral cortex, and hippocampus, which may provide a potential marker for the diagnosis of PD.

Conclusions

In summary, we have developed a NIR fluorescent probe (**DDAO-Cu**) specifically designed for imaging Cu^{2+} in the mouse brain. The probe can be facilely synthesized and exhibits excellent turn-on NIR fluorescence, remarkable sensitivity, and high selectivity towards Cu^{2+}. Furthermore, we successfully applied **DDAO-Cu** for the visual semi-quantitative detection of Cu^{2+} in living cells and zebrafish, revealing elevated Cu^{2+} levels in both cellular and zebrafish PD models. Notably, owing to its appropriate log *P* and low molecular weight, **DDAO-Cu** possesses the ability to cross the BBB, which can effectively image Cu^{2+} in MPTP-induced PD mouse models, revealing significant overall increases in Cu^{2+} levels. The ex-imaging data showed that Cu^{2+} was enriched in the cortex, hippocampus, and striatum during the advanced stages of Parkinson's disease, but suppressed in the SN region. Therefore, there is reason to believe that the Cu^{2+} level in PD is overall elevated. Altogether, this work represents a valuable tool for imaging and quantifying Cu^{2+} levels, which might help reveal the intricate role of Cu^{2+} in PD pathology.

Data availability

The authors confirm that the data supporting the findings of this study are available within the article [and/or its ESI†].

Author contributions

J. C. carried out the experiments, analyzed the data, and wrote the original manuscript. R. L., S. L., J. S., T. W. and S. X. analyzed the data and participated in the discussion. L. X. and Q. Y. performed review & editing and project administration. S. F. and G. F. supervised the whole project & guided writing, reviewed, and edited the manuscript. All authors discussed the results and co-wrote the manuscript.

Conflicts of interest

There are no conflicts to declare.

Acknowledgements

This work was supported the Natural Science Foundation of Hubei Province (2023AFB376) and the National Natural Science Foundation of China (22077044).

References

1 B. R. Bloem, M. S. Okun and C. Klein, *Lancet*, 2021, **397**, 2284–2303.
2 Z. Zeng, Y. Cen, L. Xiong, G. Hong, Y. Luo and X. Luo, *Biol. Trace Elem. Res.*, 2024, **202**, 955–964.
3 E. O. Olufunmilayo, M. B. Gerke-Duncan and R. M. D. Holsinger, *Antioxidants*, 2023, **12**, 517.
4 Y. Li, C. Yang, S. Wang, D. Yang, Y. Zhang, L. Xu, L. Ma, J. Zheng, R. B. Petersen, L. Zheng, H. Chen and K. Huang, *Int. J. Biol. Macromol.*, 2020, **163**, 562–573.
5 R. Rasia, C. Bertoncini, D. Marsh, W. Hoyer, D. Cherny, M. Zweckstetter, C. Griesinger, T. Jovin and C. Fernández, *Proc. Natl. Acad. Sci. U. S. A.*, 2005, **102**, 4294–4299.
6 P. Dusek, P. M. Roos, T. Litwin, S. A. Schneider, T. P. Flaten and J. Aaseth, *J. Trace Elem. Med. Biol.*, 2015, **31**, 193–203.
7 H. Pall, A. Williams, D. Blake, J. Lunec, J. Gutteridge, M. Hall and A. Taylor, *Lancet*, 1987, **1**, 238–241.
8 A. D. Surowka, P. Wrobel, D. Adamek, E. Radwanska and M. Szczerbowska-Boruchowska, *Metallomics*, 2015, **7**, 1522–1531.
9 R. V. Timoshenko, P. V. Gorelkin, A. N. Vaneev, O. O. Krasnovskaya, R. A. Akasov, A. S. Garanina, D. A. Khochenkov, T. M. Iakimova, N. L. Klyachko, T. O. Abakumova, V. S. Shashkovskaya, K. D. Chaprov, A. A. Makarov, V. A. Mitkevich, Y. Takahashi, C. R. W. Edwards, Y. E. Korchev and A. S. Erofeev, *Anal. Chem.*, 2024, **96**, 127–136.
10 E. Falcone, M. Okafor, N. Vitale, L. Raibaut, A. Sour and P. Faller, *Chem. Rev.*, 2021, **433**, 213727.
11 S. Wang, G. Yu, Y. Ma, Z. Yang, Y. Liu, J. Wang and X. Chen, *ACS Appl. Mater. Interfaces*, 2019, **11**, 1917–1923.
12 M. Tian, Y. Ma and W. Lin, *Acc. Chem. Res.*, 2019, **52**, 2147–2157.
13 H. Li, H. Kim, F. Xu, J. Han, Q. Yao, J. Wang, K. Pu, X. Peng and J. Yoon, *Chem. Soc. Rev.*, 2022, **51**, 1795–1835.
14 M. Yan, H. Fang, X. Wang, J. Xu, C. Zhang, L. Xu and L. Li, *Sens. Actuators, B*, 2021, **328**, 129003.
15 L. Gao, W. Wang, X. Wang, F. Yang, L. Xie, J. Shen, M. A. Brimble, Q. Xiao and S. Q. Yao, *Chem. Soc. Rev.*, 2021, **50**, 1219–1250.
16 L. Zhang, S. Peng, J. Sun, J. Yao, J. Kang, Y. Hu and J. Fang, *Chem. Sci.*, 2017, **8**, 2966–2972.
17 Q. Sun, J. Xu, C. Ji, M. Shaibani, Z. Li, K. Lim, C. Zhang, L. Li and Z. Liu, *Anal. Chem.*, 2020, **92**, 4038–4045.
18 Z. Zheng, S. Gong, J. Zhang, Y. Liu and G. Feng, *Sens. Actuators, B*, 2023, **397**, 134654.
19 Y. Liu, L. Teng, B. Yin, H. Meng, X. Yin, S. Huan, G. Song and X. B. Zhang, *Chem. Rev.*, 2022, **122**, 6850–6918.
20 D. R. Brown, K. F. Qin, J. W. Herms, A. Madlung, J. Manson, R. Strome, P. Fraser, T. Kruck, A. Bohlen, W. Schulz-Schaeffer, A. Giese, D. Westaway and H. Kretzschmar, *Nature*, 1997, **290**, 684–687.
21 Q. Xia, S. Feng, D. Liu and G. Feng, *Sens. Actuators, B*, 2018, **258**, 98–104.
22 L. V. Rubinstein, R. H. Shoemaker, K. D. Paull, R. M. Simon, S. Tosini, P. Skehan, D. A. Scudiero, A. Monks and M. R. Boyd, *J. Natl. Cancer Inst.*, 1990, **82**, 1113–1117.
23 P. Caboni, T. B. Sherer, N. Zhang, G. Taylor, H. M. Na and J. Greenamyre, *Chem. Res. Toxicol.*, 2004, **17**, 1540–1548.
24 Z. Fang, Z. Su, W. Qin, H. Li, B. Fang, W. Du, Q. Wu, B. Peng, P. Li, H. Yu, L. Li and W. Huang, *Chin. Chem. Lett.*, 2020, **31**, 2903–2908.

© 2024 The Author(s). Published by the Royal Society of Chemistry

Open Access Article. Published on 22 July 2024. Downloaded on 1/15/2026 9:18:38 PM.
This article is licensed under a Creative Commons Attribution-NonCommercial 3.0 Unported Licence.

25 B. Do Van, F. Gouel, A. Jonneaux, K. Timmerman, M. Gelé, P. Pétrault, M. Bastide, C. Laloux, C. Moreau, R. Bordet, D. Devos and J. Devedjian, *Neurobiol. Dis.*, 2016, **94**, 169–178.
26 Z. Zhou, S. Chen, Y. Huang, B. Gu, J. Li, C. Wu, P. Yin, Y. Zhang and H. Li, *Biosens. Bioelectron.*, 2022, **198**, 113858.
27 Y. Liu, X. Yang, Z. Li, Z. Liu, D. Cheng, Y. Wang, X. Wen, J. Hu, J. Liu, L. Wang and H. Wang, *CNS Neurosci. Ther.*, 2014, **20**, 76–85.
28 N. Jha, O. Jurma, G. Lalli, Y. Liu, E. Pettus, J. Greenamyre, R. Liu, H. Forman and J. Andersen, *J. Biol. Chem.*, 2000, **275**, 26096–26101.
29 P. Kabiraj, C. Valenzuela, J. Marin, D. Ramirez, L. Mendez, M. Hwang, A. Varela-Ramirez, K. Fenelon, M. Narayan and P. Skouta, *Protein J.*, 2015, **34**, 349–358.
30 K. Ito, Y. Eguchi, Y. Imagawa, S. Akai, H. Mochizuki and Y. Tsujimoto, *Cell Death Discovery*, 2017, **3**, 17013.
31 R. D'Amato, Z. Lipman and S. Snyder, *Science*, 1986, **231**, 987–989.
32 A. Mandir, S. Przedborski, V. Jackson-Lewis, Z. Wang, C. Simbulan-Rosenthal, M. Smulson, B. Hoffman, D. Guastella, V. Dawson and T. Dawson, *Proc. Natl. Acad. Sci. U. S. A.*, 1999, **96**, 5774–5779.
33 M. Ugrumov, V. Khaindrava, E. Kozina, V. Kucheryanu, E. Bocharov, G. Kryzhanovsky, V. Kudrin, V. Narkevich, P. Klodt, K. Rayevsky and T. Pronina, *Neuroscience*, 2011, **181**, 175–188.
34 K. Wu, X. Wang, L. Gong, X. Zhai, K. Wang, X. Qiu, H. Zhang, Z. Tang, H. Jiang and X. Wang, *Biosens. Bioelectron.*, 2023, **237**, 115521.
35 H. Fu, M. Cui, L. Zhao, P. Tu, K. Zhou, J. Dai and B. Liu, *J. Med. Chem.*, 2015, **58**, 6972–6983.
36 Y. Cui, X. Wang, Z. Jiang, C. Zhang, Z. Liang, Y. Chen, Z. Liu and Z. Guo, *Angew. Chem., Int. Ed.*, 2023, **62**, 202214505.
37 B. Xiong, Y. Wang, Y. Chen, S. Xing, Q. Liao, Y. Chen, Q. Li, W. Li and H. Sun, *J. Med. Chem.*, 2021, **64**, 13152–13173.
38 Z. Jiang, Z. Liang, Y. Cui, C. Zhang, J. Wang, H. Wang, T. Wang, Y. Chen, W. He, Z. Liu and Z. Guo, *J. Am. Chem. Soc.*, 2023, **145**, 7952–7961.
39 N. Hada, W. J. Netzer, F. Belhassan, L. P. Wennogle and S. Gizurarson, *Eur. J. Pharm. Sci.*, 2017, **102**, 46.
40 C. Xiong, H. Ling, Q. Hao and X. Zhou, *Cell Death Differ.*, 2023, **30**, 876–884.
41 L. Chen, J. Min and F. Wang, *Signal Transduction Targeted Ther.*, 2022, **7**, 378.
42 A. Bush, *Curr. Opin. Chem. Biol.*, 2000, **4**, 184–191.
43 J. Kardos, L. Héja, Á. Simon, I. Jablonkai, R. Kovács and K. Jemnitz, *Cell Commun. Signaling*, 2018, **16**, 71.
44 Z. L. Wang, L. Yuan, W. Li and J. Y. Li, *Trends Mol. Med.*, 2022, **28**, 258–269.
45 H. S. Kwon and S. H. Koh, *Transl. Neurodegener.*, 2020, **9**, 42.
46 D. Dexter, A. Carayon, F. Javoy-Agid, Y. Agid, F. Wells, S. Daniel, A. Lees, P. Jenner and C. Marsden, *Brain*, 1991, **114**, 1953–1975.
47 Z. Jiang, C. Zhang, X. Wang, Z. Ling, Y. Chen, Z. Guo and Z. Liu, *Angew. Chem., Int. Ed.*, 2024, 202318340.